JGR Atmospheres

RESEARCH ARTICLE
10.1029/2022JD036726

Key Points:

- Latitudinal zonal partition of cosmogenic isotope production in the Earth's atmosphere is precisely modeled for different conditions
- Production by galactic cosmic rays and solar particles is important in all zones and only polar stratosphere, respectively
- The results are coupled to a climate-chemistry model and can be used for the Holocene conditions

Correspondence to:
K. Golubenko,
kseniia.golubenko@oulu.fi

Citation:
Golubenko, K., Rozanov, E., Kovaltsov, G., & Usoskin, I. (2022). Zonal mean distribution of cosmogenic isotope (^{7}Be, ^{10}Be, ^{14}C, and ^{36}Cl) production in stratosphere and troposphere. *Journal of Geophysical Research: Atmospheres*, *127*, e2022JD036726. https://doi.org/10.1029/2022JD036726

Received 4 MAR 2022
Accepted 5 AUG 2022

Zonal Mean Distribution of Cosmogenic Isotope (^{7}Be, ^{10}Be, ^{14}C, and ^{36}Cl) Production in Stratosphere and Troposphere

K. Golubenko[1], E. Rozanov[2,3], G. Kovaltsov[4], and I. Usoskin[1]

[1]Space Climate Research Unit and Sodankylä Geophysical Observatory, University of Oulu, Oulu, Finland, [2]Physikalisch-Meteorologisches Observatorium Davos and World Radiation Center, Davos, Switzerland, [3]St. Petersburg State University, St. Petersburg, Russia, [4]Ioffe Physical-Technical Institute, St. Petersburg, Russia

Abstract Cosmogenic isotopes are produced by cosmic rays mostly in the middle-low atmosphere and then take part in the complicated processes of atmospheric transport and deposition that are different for the stratosphere and troposphere. Cosmogenic isotopes are continuously produced by galactic cosmic rays (GCRs) with a hard energy spectrum and sporadically by solar energetic particles (SEPs) with much softer energy spectra. The partition of the isotope production between the stratosphere and troposphere in different latitudinal zones depends on the spectrum of cosmic rays, geomagnetic shielding, and the tropopause shape. The exact zonal distribution of the isotope production is not accurately known and needs to be precisely modeled as well as the isotopes' transport and deposition in climatic reconstruction. Here, we present the results of the computations of ^{14}C, ^{36}Cl, ^{10}Be, and ^{7}Be cosmogenic isotope production in the Earth's atmosphere using the CRAC model. We provide zonal mean production rates separately for the stratosphere and troposphere in three latitudinal zones: tropical (0°–30°), midlatitude (30°–60°), and polar (60°–90°). The computations were performed for four scenarios: (a) production by GCR during a solar-cycle minimum; (b) production by GCR during a solar-cycle maximum; (c) SEP event with the hardest known spectrum (GLE#5); and (d) the strongest known soft-spectrum SEP event (GLE#24). The results confirm that, while all the latitudinal zones are relatively important for the isotopes produced by GCR, isotope production by SEPs in the tropical zone is small and can be neglected. The results are coupled to the SOCOL-AER2-BE chemistry-climate model and can be used for a simplified parametric modeling of the isotopes' atmospheric transport, for the conditions typical for the Holocene.

1. Introduction

Cosmogenic isotopes are nuclides whose main source is continuous production in the Earth's atmosphere by galactic cosmic rays (GCRs) and sporadically by solar energetic particles (SEPs) (Beer et al., 2012; Miyake et al., 2019). Other sources of these isotopes such as anthropogenic production during atmospheric nuclear weapon tests (Elmore et al., 1982) are not considered here. The isotope production rate varies in time: more/less isotope atoms are produced by GCRs during solar minimum/maximum times, respectively (Masarik & Beer, 2009; Poluianov et al., 2016), while the production by SEPs only takes place during sporadic strong or extreme solar eruptive events (Schrijver et al., 2012; Usoskin et al., 2006). On longer time scales, changes of the geomagnetic field modulate the isotope production. The spatial distribution of the isotope production changes for different periods and types of events. Accordingly, it is important, for studies of the cosmogenic isotopes and their terrestrial applications, to model the isotopes' production precisely for different conditions.

Cosmogenic isotopes have a broad range of decay times from minutes (e.g., half-life of ^{39}Cl is 56 min) to millions of years ($1.388 \cdot 10^{6}$ years for ^{10}Be)—see (Chmeleff et al., 2010; Korschinek et al., 2010). Short-living isotopes decay fast and are not transported far from the production site, but transport and deposition processes are important for isotopes with the life time longer than several months. The cosmogenic isotopes are transported by air masses and subsequently diffuse to the surface of the land and the oceans (Keeling et al., 2017). Most useful cosmogenic isotopes applied for studies of solar variability, cosmic rays, and also atmospheric dynamics are ^{14}C, ^{36}Cl, ^{10}Be, and ^{7}Be (e.g., Beer et al., 2012; Leppänen et al., 2010; Wu et al., 2018).

Modeling of cosmogenic isotope production has a long history. First production models (Lal & Peters, 1967; Lingenfelter, 1963) used an empirical approach based on fitting simplified model calculations to measurements

of the isotope concentrations and inelastic nuclear collisions in the atmosphere. A later semi-analytical model by O'Brien (1979) was based on a stationary analytical approximation of the development of the GCR-induced cascade in the atmosphere in the form of the Boltzman equation. Those models were based on simplified calculations of the inelastic-collision rates and applying the mean spallation yield per one collision. An important new step in modeling the isotope production was made in pioneering work by Masarik and Beer (1999), slightly updated as Masarik and Beer (2009), who performed a Monte Carlo simulation of the GCR-initiated cascade in the atmosphere directly using cross-sections of spallation reactions instead of the average inelastic collision's efficiency. Those works were set for fixed levels of solar activity and/or spectral shapes of GCRs and cannot be used to compute the isotope production for SEP events. A more detailed approach based on the yield function (isotope production by a unit flux of monoenergetic primary CR particles) made it possible to compute the isotope production for any spectral shape, including GCR and SEP. However, earlier models of that type (Webber et al., 2007; Webber & Higbie, 2003) provided only the columnar (integrated over the entire thickness of the atmosphere) yield functions for cosmogenic isotopes making it impossible to model the altitude profile of the isotope production and, thus, to apply atmospheric transport models. This approach was further developed as the CRAC (Cosmic-Ray Atmospheric Cascade) family of numerical models (Kovaltsov et al., 2012; Kovaltsov & Usoskin, 2010; Usoskin & Kovaltsov, 2008), based on a full Monte Carlo simulation of the cosmic-ray induced cascade in the atmosphere. It includes yield functions computed for different atmospheric levels and thus, makes it possible to model the altitude profile of the isotope production and to couple it directly with the atmospheric transport models. The most recent and precise version of the CRAC model (Poluianov et al., 2016, 2020) is based on the GEANT-4 Monte-Carlo tool computing the yield functions of production of six cosmogenic isotopes, ^{14}C, ^{36}Cl, ^{10}Be, ^{7}Be, ^{22}Na, and ^{3}H in the Earth's atmosphere by energetic protons and heavier particles.

Because of the soft energy spectrum of SEPs, modeling of their contribution to the production of cosmogenic isotopes is particularly challenging as it requires accurate knowledge of the low-energy part of the production (yield) function. Attempts to reconstruct the events of solar particles in the past using measurements of cosmogenic isotopes have been repeatedly made. Simpson (1960) argued that intense fluxes of solar energetic protons can produce Triton (or Tritium) and ^{14}C isotopes in the terrestrial atmosphere at times near the maximum of the solar activity cycle. It was shown theoretically (Usoskin & Kovaltsov, 2006; Webber et al., 2007) that extremely strong SEP events can produce cosmogenic isotopes in the amount detectable in high-resolution ^{10}Be and ^{14}C data (Usoskin et al., 2020). Such extreme SEP events were discovered recently as recorded in multiple terrestrial cosmogenic isotope (^{14}C, ^{10}Be, and ^{36}Cl) data throughout the last millennia (e.g., Brehm et al., 2021, 2022; Mekhaldi et al., 2015; Miyake et al., 2012; 2013; O'Hare et al., 2019; Paleari et al., 2022; Sukhodolov et al., 2017; Usoskin et al., 2013; Uusitalo et al., 2018).

After production with a complex 3D distribution in the atmosphere, cosmogenic isotopes experience transport and deposition processes that are specific for each isotope (Beer et al., 2012). These processes can significantly distort the production signal in the measured concentrations. For example, the 11-year solar cycles in the ^{14}C production can be greatly, by a factor of ≈100, attenuated in the measured Δ^{14}C by the global biogeochemical carbon cycle (Bard et al., 1997; Usoskin & Kromer, 2005). Transport of cosmogenic isotopes in the atmosphere can be modeled with different levels of precision and detalization, from simple assumptions of global mixing or purely regional deposition (McCracken, 2004) to full atmospheric models. The latter is particularly important for the isotopes used as tracers of the atmospheric dynamics, such as the short-living ^{7}Be isotope. For ^{14}C, multibox-diffusion models (Bard et al., 1997; Oeschger et al., 1975) are usually sufficient but a full 3D dynamical model can be used when dynamical interaction with the ocean is important (Dinauer et al., 2020; Roth & Joos, 2013). Several full dynamical models for the transport of beryllium isotopes have been developed (e.g., Field et al., 2006; Golubenko, Rozanov, Kovaltsov, et al., 2021; Heikkilä et al., 2008), but their application is complicated and requires intensive computations. As an alternative, a medium-complexity parameterization was proposed by Heikkilä, Beer, et al. (2013), where transport coefficients between large-scale zones have been computed based on the full modeling. This approach, providing a reasonable balance between simplicity and realism, has been actively used in recent studies of cosmogenic-isotope data.

Here, we present the results of modeling the production of cosmogenic isotopes ^{14}C, ^{36}Cl, ^{10}Be, and ^{7}Be in the atmosphere and provide zonal distributions (tropical, subtropical, and polar regions) in the stratosphere and troposphere. A combination of a numerical model of cosmogenic isotopes production with the chemical climate model (CCM) SOCOL-AER2-BE (Golubenko, Rozanov, Kovaltsov, et al., 2021) has been developed, where in

Table 1
Four Scenarios of Cosmogenic Isotope Production Considered Here

Scenario	CR type	Description
I.	GCR	A typical solar-cycle minimum year (specified here as 1997) with a low value of the solar modulation potential $\phi = 400$ MV.
II.	GCR	A typical solar-cycle maximum year (specified as 2000) with $\phi = 1100$ MV.
III.	SEP	The strongest directly measured soft-spectrum SEP event (specified as ground-level enhancement, GLE#24 of 04-Aug-1972).
IV.	SEP	The strongest directly measured hard-spectrum SEP event of 23-Feb-1956 (GLE#5).

situ production of the isotopes by cosmic (solar and galactic) rays is included explicitly. This will advance our ability to reconstruct energy spectra of extreme SEP events based on cosmogenic-isotope data and increase the accuracy of the spectra reconstruction, which is of great importance for studies of solar-terrestrial relationships.

2. Model Description

Production of ^{14}C, ^{36}Cl, ^{10}Be, and ^{7}Be isotopes was computed using the tabulated yield functions computed using the CRAC model by Poluianov et al. (2016). The CRAC model is the most recent and accurate model of cosmogenic isotope production, based on the GEANT4 Monte Carlo simulation tool (Agostinelli et al., 2003), which models the nucleonic-muon-electromagnetic cascade induced by primary cosmic-ray particles in the atmosphere. The model provides a set of precisely computed yield functions for the production of cosmogenic isotopes for different primary particle types (viz. protons and α-particles, the latter effectively representing all heavier species), energy, and atmospheric depths. The isotope's production rate is presented as a function of the location (via the geomagnetic rigidity cutoff—see Cooke et al., 1991; Herbst et al., 2013), atmospheric height (via the residual atmospheric depth or barometric pressure), and time (via the time-variable energy spectrum). These production rates are further used as input parameters for the CCM SOCOL-AER2-BE model to properly account for the realistic tropopause, which varies greatly in time and to provide an accurate partition between stratospheric and tropospheric productions.

The CCM SOCOL-AER2-BE (chemistry-climate model SOlar Climate Ozone Links with aerosol and Beryllium modules) is based on the SOCOL-AER2 model (Feinberg et al., 2019) extended with the beryllium module (Golubenko, Rozanov, Kovaltsov, et al., 2021). This model version consists of the general circulation model MA-ECHAM5 (Hommel et al., 2011) and the atmospheric chemistry module MEZON (Model for investigating ozone trends) (Egorova et al., 2003), interacting with each other every two modeling hours. In this study, the MA-ECHAM5 dynamic is nudged toward the meteorological data from fifth-generation ECMWF (European Center for Medium-Range Weather Forecasts) atmospheric reanalysis data of the global climate ERA-Interim (eraiaT42L39) reanalyses (Hersbach et al., 2020). The CCM SOCOL-AER2-BE utilizes the Gaussian transform horizontal grid with the T42 triangular truncation (64 latitudes and 128 longitudes) splitting the model space into grid cells of about 2.8° × 2.8° size. The model's vertical-direction grid consists of 39 levels in the hybrid sigma-pressure coordinate system covering the altitudes ranging from the ground surface to about 80 km (0.01 hPa) (Stenke et al., 2013). For all the considered isotopes, we use a similar scheme of production as in the CCM SOCOL-AER2-BE.

The model was run for the four scenarios described in Table 1.

For scenarios I and II, the isotope production was calculated for GCR with the spectrum parameterized via force-field approximation following the procedure described elsewhere (Koldobskiy et al., 2019; Usoskin et al., 2005, 2011). The force-field approximation describes the GCR spectrum with a single parameter, called the modulation potential ϕ, which is usually defined empirically from the data of the ground-based network of neutron monitors (e.g., Usoskin et al., 2005). The exact value of the modulation potential depends on the model assumptions (Herbst et al., 2010), but is uniquely defined within a given model. Here, we used the force-field model as defined by Usoskin et al. (2011) with the reference proton local interstellar spectrum by Vos and Potgieter (2015). The contribution of helium and heavier species has been explicitly considered following the methodology validated using direct space-borne measurements of GCR spectra by AMS02 experiment (Koldobskiy et al., 2019).

For scenarios III and IV, spectra of SEPs were considered according to the model by Koldobskiy et al. (2021). The spectra represent the total event-integrated fluences of SEPs obtained by fitting the Band-type spectral shape to the data from the ground-based neutron-monitor network and the space-borne detectors.

The geomagnetic field was set for all scenarios according to the IGRF (International Geomagnetic Reference Field) model (Thébault et al., 2015) for epoch 2000 and quiet-Sun conditions (Kp = 0).

Table 2
Zones of Isotope Productions Considered Here

Zone	Notation	Hemisphere	latitudes	region	Notation	Hemisphere	latitudes	region
Polar	N3s	North	60°–90°	strato	S3s	South	60°–90°	strato
Polar	N3t	North	60°–90°	tropo	S3t	South	60°–90°	tropo
Mid-lat	N2s	North	30°–60°	strato	S2s	South	30°–60°	strato
Mid-lat	N2t	North	30°–60°	tropo	S2t	South	30°–60°	tropo
Tropics	N1s	North	0°–30°	strato	S1s	South	0°–30°	strato
Tropics	N1t	North	0°–30°	tropo	S1t	South	0°–30°	tropo

For calculations, the tropopause height was defined in the CCM modeled meteorological data according to the World Meteorological Organization (WMO) as the lowest level where the absolute value of the temperature lapse rate decreases to 2K/km or less, with the average lapse rate between this level and all higher levels within 1.2 miles or 2 km (Santer et al., 2003). The location of tropopause was defined at each model step, namely every two model hours.

Using the models and scenario described above, we have computed the production of the four cosmogenic isotopes in the atmosphere with its partition in 12 zones, following the parameterization of Heikkilä, Beer, et al. (2013), as specified in Table 2. The zonal production was defined as an average in each zone over a year to smooth the seasonal variability of the tropopause heights.

As an example, the zonal stratospheric fraction of ^{10}Be production is shown in Figure 1 as a function of the geographical latitude in the Northern hemisphere. The red shaded area denotes the range of the values within a solar cycle, namely between scenarios I and II, at the modern geomagnetic field conditions (the geomagnetic dipole moment $M = 7.8 \cdot 10^{22}$ A m^2). The latitudinal profile of the stratospheric fraction appears fairly stable against the solar activity and geomagnetic field variations. The latter is represented by the full-range variability of the value of M during the Holocene (e.g., Usoskin et al., 2016), between $6 \cdot 10^{22}$ (blue dash-dotted curve) and $12 \cdot 10^{22}$ A m^2 (green dashed curve). The stratospheric fraction appears robust against these changes and thus can be applied to the entire Holocene. For comparison, the same zonal stratospheric fraction of ^{10}Be production is shown for earlier computations (fig. 7 of Masarik & Beer, 1999) that yields significantly higher stratospheric production. The reason for this discrepancy is not known as discussed below.

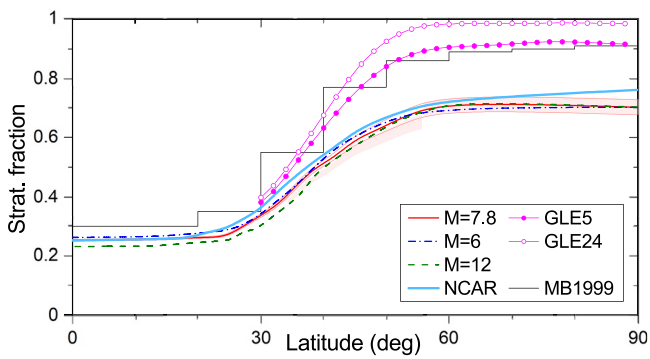

Figure 1. Zonal stratospheric fraction of the ^{10}Be isotope production by GCR as function of the geographical latitude in the Northern hemisphere. The black dotted line corresponds to the mean modern production as depicted in fig. 7 of Masarik and Beer (1999, – MB1999). The red line represents the results obtained here for the modern geomagnetic field (dipole moment $M = 7.8 \cdot 10^{22}$ A m^2) and moderate solar activity ($\phi = 600$ MV), while the red shading covers the range of solar cycle variability between $\phi = 400$ and 1000 MV. The thick light-blue curve corresponds to the moderate modern conditions ($\phi = 600$ MV and $M = 7.8 \cdot 10^{22}$), naemly similar to the red curve, but using the NCEP/NCAR mean tropopause profile (see https://psl.noaa.gov/data/gridded/data.ncep.reanalysis.html). Blue dash-dotted and green dashed curves correspond to the moderate solar activity ($\phi = 600$ MV, red curve) at the lowest ($M = 6 \cdot 10^{22}$ A m^2) and highest ($M = 12 \cdot 10^{22}$ A m^2) geomagnetic shielding during the Holocene, respectively. The cyan curves with open and filled circles correspond to the soft- (scenario III) and hard- (scenario IV) SEP events, respectively.

3. Results

3.1. Zonal Production

Using the model described above, we have computed the mean production rates of the isotopes (^{10}Be, ^{7}Be, ^{36}Cl, and ^{14}C) for the four scenarios (Table 1). The global annual production and its partition over the geographical zones (see Table 2) are summarized in Tables 3–6.

Table 3 presents the zonal partition of the ^{10}Be production. One can see that 40%–43% of the isotope is produced by GCR (scenarios I and II) in the troposphere. The tropospheric production fraction is slightly greater for scenario II than for scenario I because of the harder GCR spectrum around the solar maximum. About half of the global isotope production is produced in the midlatitude zones N2+S2, which provide a balance between the area (the polar zone is small in size) and geomagnetic shielding, which is maximal in the tropical zone. More beryllium is produced in the tropical troposphere than in the tropical stratosphere, in agreement with earlier studies (e.g., Heikkilä et al., 2009). This can be explained by a combination of the high tropopause altitude (see, e.g., Figure 2) and the high geomagnetic rigidity

Table 3
The Global Annual (for Scenarios I and II) and Event-Integrated (for Scenarios II and IV) Averaged Production Q_{glob} of ^{10}Be and the Percentage of Its Zonal Production (see Table 2) for the Four Scenarios (see Table 1) Considered Here

Scenario	Q_{glob}	Sphere	%	S3	S2	S1	N1	N2	N3
I.	1.61 E+17	tropo-	40.32	2.9	9.08	7.54	8.41	9.26	3.13
	atoms/s	strato-	59.68	11.31	14.86	2.78	3.13	17.25	10.36
II.	1.30 E+17	tropo-	43.19	2.82	9.47	8.69	9.62	9.56	3.03
	atoms/s	strato-	56.81	9.97	14.43	3.16	3.54	16.56	9.14
III.	8.08 E+22	tropo-	1.23	0.61	0.09	0.00	0.00	0.27	0.32
	atoms	strato-	98.77	41.71	5.33	0.00	0.00	15.03	36.65
IV.	3.04 E+23	tropo-	8.25	2.61	1.36	0.01	0.02	2.52	1.7
	atoms	strato-	91.75	32.20	11.74	0.00	0.01	18.31	29.52

cutoff (high-energy CR particles have higher penetrating abilities). The tropospheric production computed here is systematically greater than 31%–35% reported earlier (Heikkilä, Beer et al., 2013; Heikkilä, Muscheler, et al., 2013; Miyake et al., 2019). This difference is also seen in Figure 1 where the stratospheric production fraction computed here (red curve) is systematically lower than that from Masarik and Beer (1999). Since the earlier models are non-transparent, the exact origin of the difference is unclear and lies outside of the scope of this paper: it can be due to the different GCR spectra applied here and by Masarik and Beer (1999), different account for helium and heavier species, different tropopause height profiles, and so on. To check the influence of the exact tropopause height on the stratospheric production fraction, we compared the computed fractions for ^{10}Be production for the ERA-Interim and NCAR tropopause profiles as shown in Figure 1 by red and blue curves, respectively.

The results suggest that the often used tropo/strato-sphere production ratio of (30–40)/(70–60) for ^{10}Be should be revisited to (40–45)/(60–55) for GCR, but the exact ratio depends on the used model profile tropopause. We note that our results are based upon a realistic data-driven ERA-Interim model. For the SPE scenarios III and IV, most of the isotope production takes place in the polar stratosphere even for a hard-spectrum SEP (scenario IV) in agreement with earlier results (e.g., Mekhaldi et al., 2021). The global tropospheric production of ^{10}Be is small, only 1%–10% of the global production for SEP events, depending on the energy spectrum—the softer the spectrum is, the smaller is the tropospheric fraction.

Qualitatively similar conclusions hold for the production of ^{7}Be (Table 4) and ^{36}Cl (Table 5), but the tropospheric fraction is slightly smaller than that for ^{10}Be because of the lower effective energy of their production (Asvestari et al., 2017; Koldobskiy et al., 2022). On the other hand, the tropospheric production reaches nearly half for ^{14}C for GCR since ^{14}C is produced mostly by atmospheric neutrons whose maximum concentration lies in the upper troposphere.

Table 4
The Same as Table 3 but for ^{7}Be

Scenario	Q_{glob}	sphere	%	S3	S2	S1	N1	N2	N3
I.	3.64 E+17	tropo-	35.23	2.34	7.79	6.95	7.74	7.86	2.55
	atoms/s	strato-	64.77	12.10	16.13	3.13	3.53	18.67	11.20
II.	2.92 E+17	tropo-	38.15	2.30	8.21	8.04	8.90	8.19	2.51
	atoms/s	strato-	61.85	10.67	15.72	3.58	4.02	17.98	9.88
III.	1.01 E+24	tropo-	0.08	0.04	0.01	0.00	0.00	0.02	0.02
	atoms	strato-	99.92	45.48	2.16	0.00	0.00	11.76	40.51
IV.	9.68 E+23	tropo-	3.99	1.21	0.69	0.01	0.01	1.29	0.78
	atoms	strato-	96.01	35.68	10.25	0.00	0.01	17.85	32.23

Table 5
The Same as Tables 3 and 4 but for ^{36}Cl

Scenario	Q_{glob}	sphere	%	S3	S2	S1	N1	N2	N3
I.	1.41 E+16	tropo-	40.73	2.97	9.22	7.53	8.39	9.42	3.20
	atoms/s	strato-	59.27	11.39	14.67	2.70	3.04	17.07	10.41
II.	1.13 E+16	tropo-	43.67	2.90	9.62	8.69	9.62	9.74	3.10
	atoms/s	strato-	56.33	10.00	14.25	3.08	3.45	16.39	9.15
III.	2.85 E+22	tropo-	0.21	0.01	0.03	0.00	0.00	0.07	0.10
	Atoms	strato-	99.79	44.93	2.66	0.00	0.00	12.29	39.83
IV.	3.50 E+22	tropo-	6.58	1.62	1.36	0.01	0.01	1.86	1.72
	Atoms	strato-	93.42	35.16	9.84	0.00	0.01	17.62	30.80

The zonal production results can be summarized as follows:

1. the tropospheric fraction of the global isotope production ranges between 40% and 50% for GCR depending on the isotope and the level of solar modulation of GCR, which is systematically higher than 30%–40% used previously;
2. the tropospheric fraction is small, 0.2%–12% for SEP depending on the hardness of the SEP spectrum;
3. isotopes are mostly produced at midlatitudes for GCR and in polar regions by SEPs.

3.2. Latitude-Altitude Production Profiles

The altitude-latitude profiles of the cosmogenic isotope ^{7}Be zonal-mean production rates for the four scenarios are shown in Figure 2. One can see that the maximum production by GCR (scenarios I and II) takes place in the mid/high-latitude stratosphere nearly independently on altitude above the 100 hPa pressure level and decreases towards the surface. During GLE events (scenarios III and IV), the maximum production is in the upper polar stratosphere (above the 10 hPa level) with no (scenario III) or little (scenario IV) production in the mid/tropical zone. Qualitatively very similar profiles were obtained for ^{10}Be and ^{36}Cl isotopes. However, the profiles for ^{14}C (Figure 3) look significantly different: the maximum of production is confined in the altitude range of 50–200 hPa (so-called Pfotzer maximum) for the GCR scenarios I and II and 10–40 hPa for the SEP scenarios II and IV. This difference in the shape, between pillar-like and bra-like distributions, is defined by the different physical mechanisms of the isotope production. On the one hand, the isotope ^{14}C is produced mostly via the (n, p)-reaction (often called neutron capture), where neutrons are secondary products of the cosmic-ray induced atmospheric cascade. Accordingly, the production requires the nucleonic cascade to be fully developed in the atmosphere, with the maximum corresponding to the pressure level of 100–200 hPa (Dorman, 2004). On the other hand, isotopes ^{7}Be, ^{10}Be, and ^{36}Cl are produced as a result of spallation reactions, which can be induced also by primary cosmic rays without full development of the atmospheric cascade.

Table 6
The Same as Tables 3–5 but for ^{14}C

Scenario	Q_{glob}	sphere	%	S3	S2	S1	N1	N2	N3
I.	8.73 E+18	tropo-	46.87	3.43	10.57	8.71	9.67	10.81	3.68
	atoms/s	strato-	53.13	10.31	13.25	2.27	2.54	15.49	9.27
II.	7.10 E+18	tropo-	49.68	2.30	8.21	8.04	8.90	8.19	2.51
	atoms/s	strato-	50.32	9.10	12.81	2.56	2.85	14.82	8.19
III.	3.60 E+24	tropo-	2.06	1.04	0.14	0.00	0.00	0.45	0.54
	atoms	strato-	97.94	41.55	5.04	0.00	0.00	14.59	36.66
IV.	1.41 E+25	tropo-	12.05	3.84	1.93	0.01	0.02	3.60	2.49
	atoms	strato-	87.95	30.67	11.54	0.00	0.01	17.50	28.39

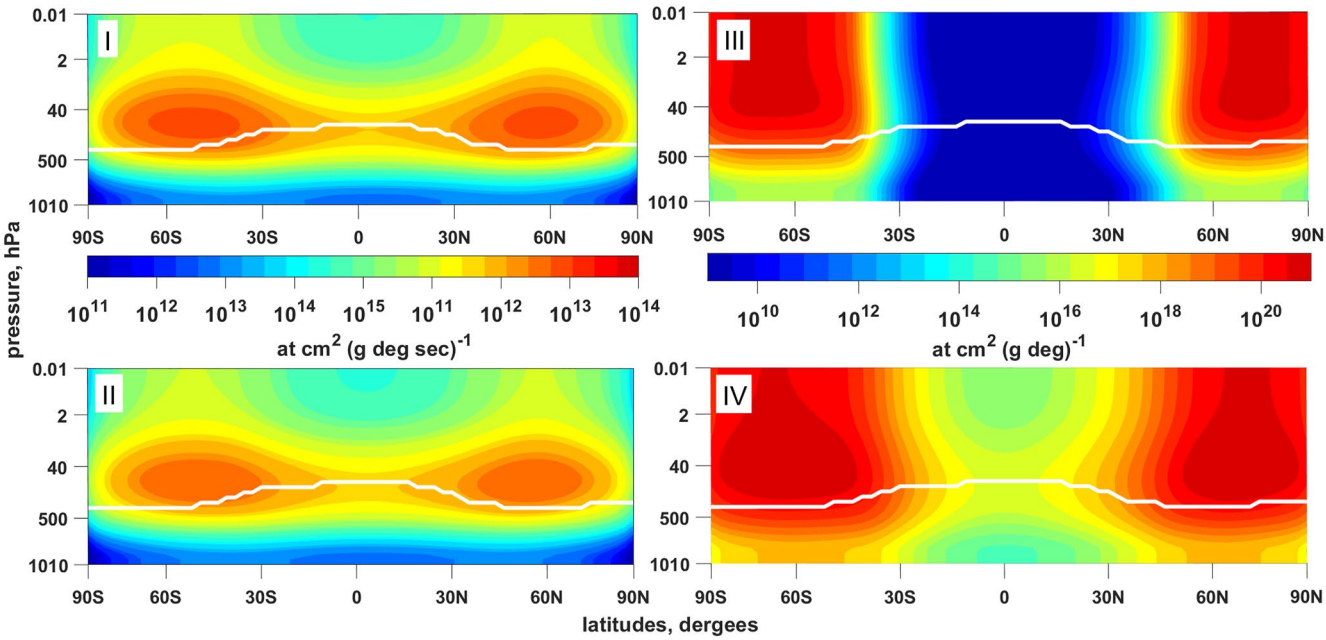

Figure 2. Zonal mean production rates of ^{7}Be as a function of geographical latitude and model's atmospheric pressure level for different scenarios (see Table 1) (for I and II: in atoms per second per degree of latitude per g/cm^2 of air; for III and IV: in atoms per degree of latitude per g/cm^2 of air). The tropopause height averaged over the period of 1996–2008 is depicted by the white line. Digital tables for these plots are available elsewhere (see Data Availability Statement).

3.3. The Role of Tropopause

Although the cosmogenic-isotope production looks fairly symmetric between the two hemispheres (e.g., Figure 2), there are essential differences in the zonal partitions (see Tables 3–6). This is related, to large extent, to the actual tropopause height, as we discuss in more detail here.

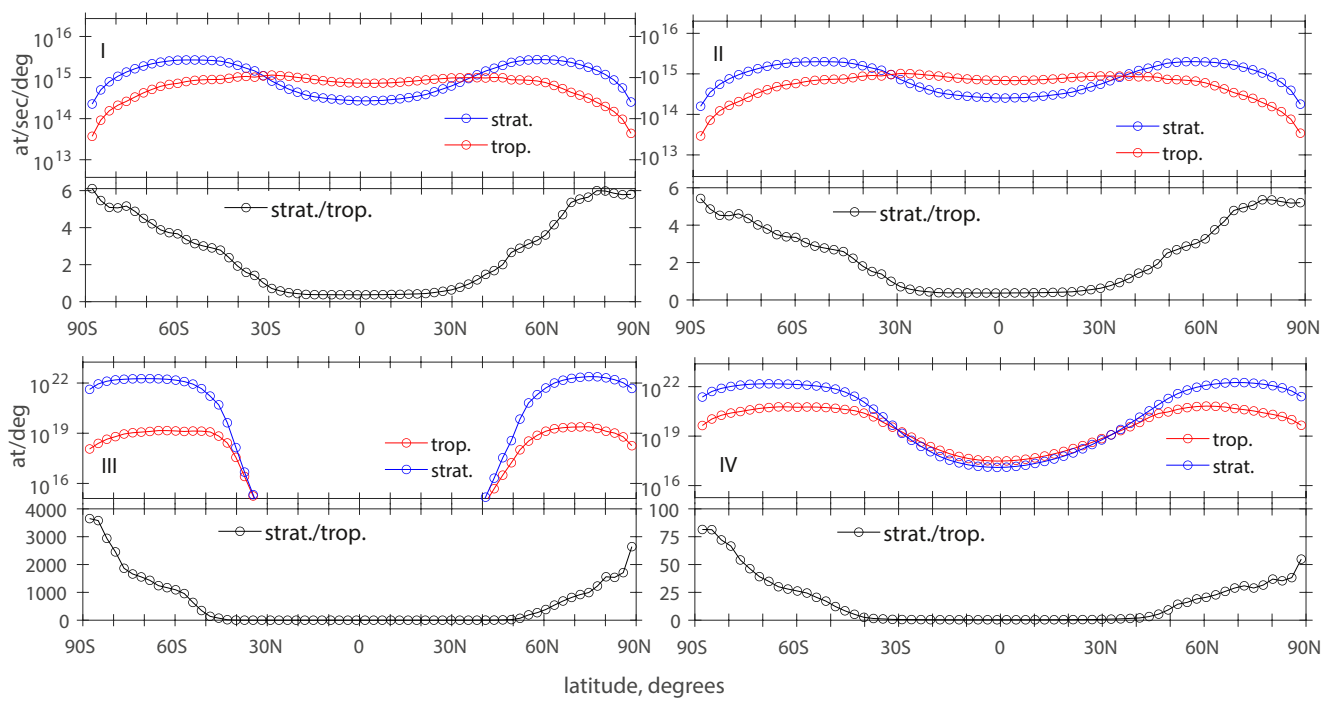

Figure 3. The same as Figure 2 but for ^{14}C. Digital tables for these plots as well as for ^{7}Be and ^{36}Cl productions are given in Data Availability Statement.

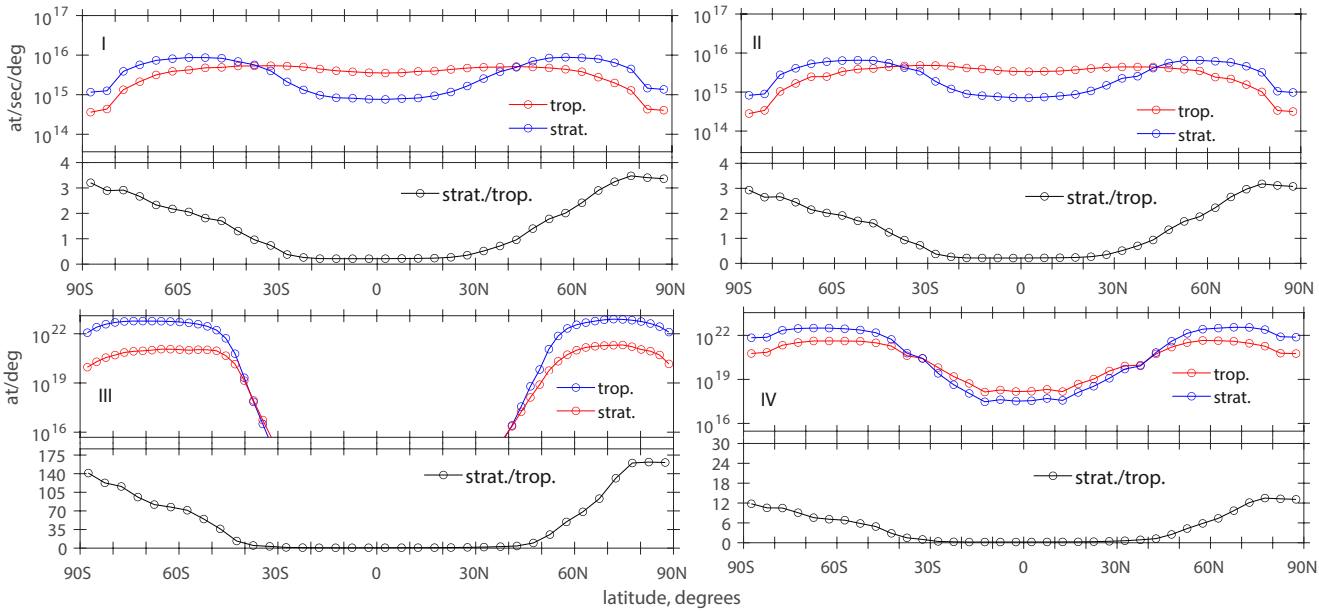

Figure 4. Zonal mean production rates of ^{7}Be for the four scenarios (Table 1) Upper sub-panels depict the stratospheric (blue) and tropospheric (red) zonal mean (per latitude degree) production rates, while lower panels show the stratospheric-to-tropospheric production ratio.

The tropopause height is not uniform over the globe. On average, it is higher, being 16–18 km in the tropical regions, and lower (7–10 km) in polar caps, as shown, for example, in Figure 2, and can vary significantly between different seasons. In this work, we use the dynamically modeled tropopause for the period 1997–2008. It has been shown that there is a systematic change in the tropopause height of about 50 m per decade as related to the global change (Meng et al., 2021) but we neglect this effect here. This result can be considered as approximate if applied to other periods (cf. Heikkilä, Beer, et al., 2013; Heikkilä et al., 2009). In the case of significantly different conditions, for example, ice ages or geomagnetic reversals/excursions, full modeling needs to be provided, which is beyond the scope of this work.

The zonal mean productions of ^{7}Be, ^{14}C, ^{10}Be, and ^{36}Cl are shown in Figures 4–7 separately for the stratosphere and troposphere for the four scenarios along with the ratio of the stratospheric to tropospheric productions.

One can see that the profiles of the stratospheric and tropospheric productions are different. For the GCR scenarios I and II, the tropospheric production has a broad maximum within the tropical and midlatitude regions, but the stratospheric production has peaks at higher latitudes of about 60°. This leads to the dominance of the tropospheric production in the tropical region. These profiles are formed by an interplay between three effects: (a) the geomagnetic shielding which reduces the production rate from the poles to the equator; (b) the geometrical factor related to the area which increases from poles to the equator; and (c) the latitudinal profile of the tropopause which nearly halves the stratospheric thickness in the tropics with respect to the polar regions. As a result, the two latter factors (b) and (c) compensate the first one for the GCR-related tropospheric production, leading to a broad maximum, but both factors (a) and (c) lead to a large reduction of the polar tropospheric production, and the factor (b) alone is insufficient to compensate for it.

The situation is different for the SEP-based scenarios III and IV. The production occurs mostly in the (sub)polar stratospheres with the stratosphere-to-troposphere production ratio varying between about 15 (^{14}C for scenario IV) and 3000 (^{7}Be for scenario III). The isotope production is greatly suppressed in the tropical zone at latitudes below ≈40°. This is mostly driven by the soft spectrum of SEP in comparison with that of GCR so that most of the production occurs in the polar stratosphere.

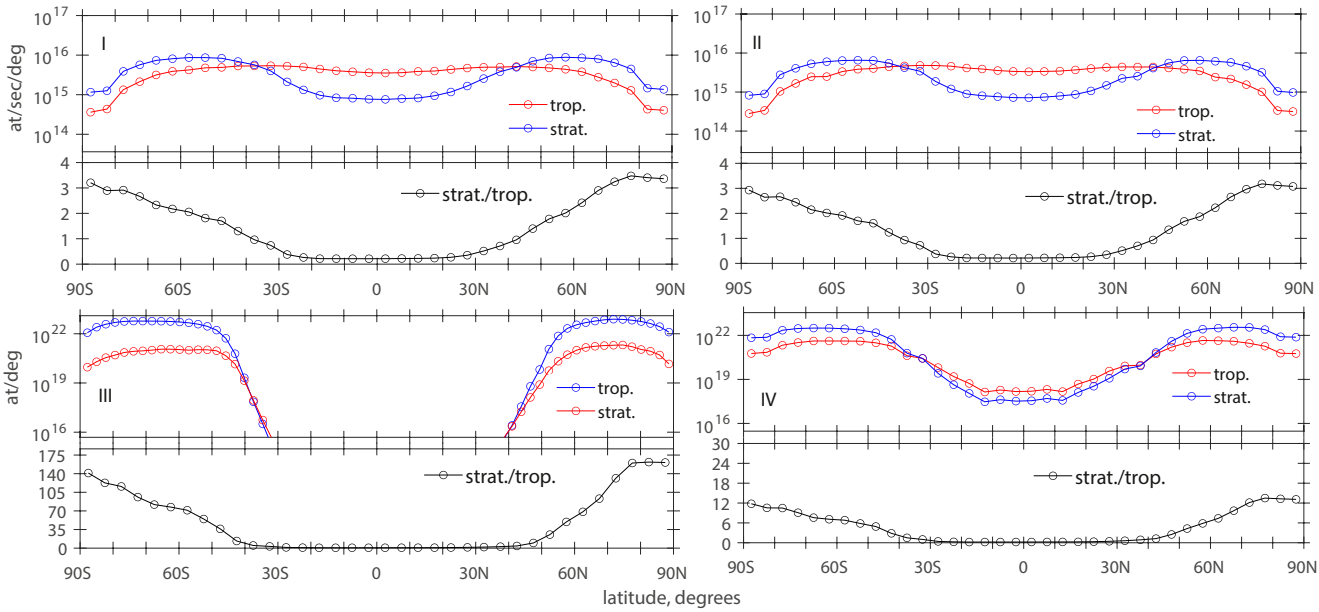

Figure 5. The same as Figure 4 but for ^{14}C.

4. Discussion and Conclusions

Full comprehensive modeling of cosmogenic isotopes production by cosmic rays in the Earth's atmosphere is well developed (Poluianov et al., 2016) and applied to state-of-the-art studies of atmospheric dynamics, paleoclimate, paleomagnetism, solar variability, and so on. Such models are laborious, computationally heavy, and not-easy-to-use and are usually applied on a case-by-case basis. On the other hand, sometimes quick yet reliable estimates are needed without complicated and expensive model runs. Such estimates often come via simplified parameterizations which can be straightforwardly applied in atmospheric models.

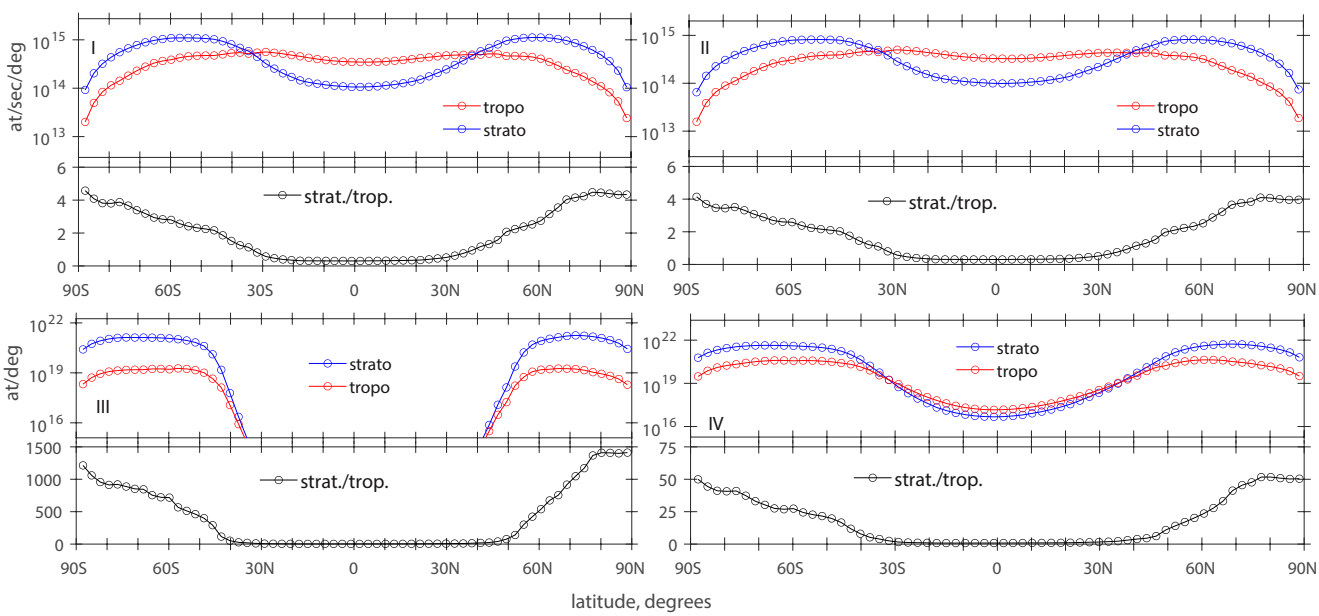

Figure 6. The same as Figure 4 but for ^{10}Be.

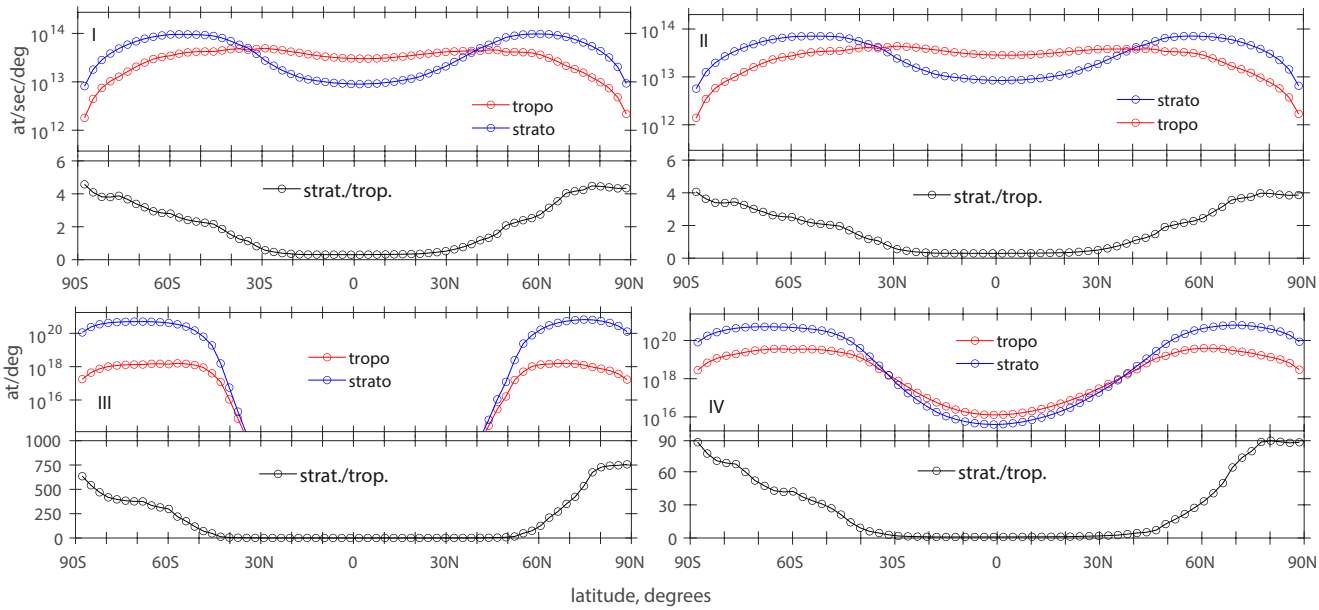

Figure 7. The same as Figure 4 but for ^{36}Cl.

Here, we present a simple parameterization of cosmogenic isotope production partitioned in different atmospheric regions/zones that is important for large-scale transport and deposition of the isotopes using full 3D modeling. The results are presented in Tables 3–6 and can be summarized as follows.

1. For GCR (scenarios I and II), the global fraction of stratospheric production is 50%–60% which is smaller than previously used 60%–70%, implying that the tropospheric production is more important than considered earlier. In particular, the tropospheric production dominates in the tropical regions. This is likely related to more accurate modeling, including both the isotope production and the realistic dynamical tropopause, as discussed above.
2. The relative percentage of zonal productions does not change much for solar-minimum and solar-maximum GCR conditions (scenarios I and II, respectively), while the global production rates changes by 15%–20% over a solar cycle.
3. For SEP scenarios III and IV, most of the cosmogenic-isotope atoms are produced in the polar regions (>60% and >80% for hard- and soft-spectrum events, respectively), in agreement with earlier studies (e.g., Mekhaldi et al., 2021). Isotope production by SEPs in the tropical zone is small (<0.05%) and can be neglected.
4. Accordingly, for simple estimates, the polar stratospheric production of cosmogenic isotopes can be assumed for SEP events with the accuracy of the assumption to be within 10%–20%.
5. The result computed here for the modern-epoch conditions is approximately valid also for the entire Holocene conditions with the stable climate and variable solar modulation and geomagnetic shielding. Extension beyond the Holocene is not recommended since the tropopause might have a different profile. Neither can this result be directly applied to the period of geomagnetic reversals or excursions, when the geomagnetic shielding cannot be represented by an eccentric dipole approximation.

These results can be used for a parametric fast estimate, without explicit modeling, of the relation between the isotope production and measurements, for example, in the way proposed by Heikkilä, Beer, et al. (2013).

Data Availability Statement

[Software] CCM SOCOL-AER2-BE used for paper is preserved at https://doi.org/10.5281/zenodo.5006356 (Golubenko, Rozanov, Sukhodolov, et al., 2021). [Data set] Cosmogenic isotopes production (14C, 36Cl, 10Be, and 7Be) via CCM SOCOL-AERv2-BE: https://doi.org/10.5281/zenodo.6852523 (Golubenko et al., 2022).

Acknowledgments
This work was partly supported by the Academy of Finland (Projects ESPERA no. 321882) and the Vilho, Yrjö, and Kalle Väisälä Foundation of the Finnish Academy of Science and Letters (scholarship of KG). The maintenance and development of the SOCOL model is supported by SNSF Grant 200020-182239 (POLE). Eugene Rozanov work on the SOCOL model adaptation and application was partly performed in the SPbSU "Ozone Layer and Upper Atmosphere Research laboratory" supported by grant from Ministry of Science and Higher Education under agreement 075-15-2021-583 and RSF Grant 20-67-46016. The work benefited from the discussions in the framework of the International Space Science Institute (ISSI) team 510 "SEESUP—Solar Extreme Events: Setting Up a Paradigm."

References

Agostinelli, S., Allison, J., Amako, K., Apostolakis, J., Araujo, H., Arce, P., et al. (2003). GEANT4 – A simulation toolkit. *Nuclear Instruments and Methods in Physics Research, Section A*, *506*, 250–303. https://doi.org/10.1016/S0168-9002(03)01368-8

Asvestari, E., Gil, A., Kovaltsov, G. A., & Usoskin, I. G. (2017). Neutron monitors and cosmogenic isotopes as cosmic ray energy-integration detectors: Effective yield functions, effective energy, and its dependence on the local interstellar spectrum. *Journal of Geophysical Research*, *122*, 9790–9802. https://doi.org/10.1002/2017JA024469

Bard, E., Raisbeck, G., Yiou, F., & Jouzel, J. (1997). Solar modulation of cosmogenic nuclide production over the last millennium: Comparison between ^{14}c and ^{10}be records. *Earth and Planetary Science Letters*, *150*, 453–462. https://doi.org/10.1016/S0012-821X(97)00082-4

Beer, J., McCracken, K., & von Steiger, R. (2012). *Cosmogenic radionuclides: Theory and applications in the terrestrial and space environments*. Springer.

Brehm, N., Bayliss, A., Christl, M., Synal, H., Adolphi, F., Beer, J., et al. (2021). Eleven-year solar cycles over the last millennium revealed by radiocarbon in tree rings. *Nature Geoscience*, *14*, 10–15. https://doi.org/10.1038/s41561-020-00674-0

Brehm, N., Christl, M., Knowles, T. D. J., Casanova, E., Evershed, R., Adolphi, F., et al. (2022). Tree-rings reveal two strong solar proton events in 7176 and 5259 BCE. *Nature Communications*, *13*, 1196. https://doi.org/10.1038/s41467-022-28804-9

Chmeleff, J., von Blanckenburg, F., Kossert, K., & Jakob, D. (2010). Determination of the ^{10}Be half-life by multicollector ICP-MS and liquid scintillation counting. *Nuclear Instruments and Methods in Physics Research, Section B*, *268*(2), 192–199. https://doi.org/10.1016/j.nimb.2009.09.012

Cooke, D., Humble, J., Shea, M., Smart, D., Lund, N., Rasmussen, I., et al. (1991). On cosmic-ray cut-off terminology. *Nuovo Cimento della Società Italiana di Fisica - C: Geophysics and Space Physics*, *14*, 213–234. https://doi.org/10.1007/bf02509357

Dinauer, A., Adolphi, F., & Joos, F. (2020). Mysteriously high Δ14C of the glacial atmosphere: Influence of 14C production and carbon cycle changes. *Climate of the Past*, *16*(4), 1159–1185. https://doi.org/10.5194/cp-16-1159-2020

Dorman, L. (2004). *Cosmic rays in the Earth's atmosphere and underground*. Kluwer Academic Publishers.

Egorova, T., Rozanov, E., Zubov, V., & Karol, I. (2003). Model for investigating ozone trends (MEZON). *Izvestiya - Atmospheric and Oceanic Physics*, *39*, 277–292.

Elmore, D., Tubbs, L. E., Newman, D., Ma, X. Z., Finkel, R., Nishiizumi, K., et al. (1982). 36Cl bomb pulse measured in a s^{ha}llow ice core from Dye 3, Greenland. *Nature*, *300*(5894), 735–737. https://doi.org/10.1038/300735a0

Feinberg, A., Sukhodolov, T., Luo, B.-P., Rozanov, E., Winkel, L. E., Peter, T., & Stenke, A. (2019). Improved tropospheric and stratospheric sulfur cycle in the aerosol-chemistry-climate model SOCOL-AERv2. *Geoscientific Model Development*, *12*(9), 3863–3887. https://doi.org/10.5194/gmd-12-3863-2019

Field, C., Schmidt, G., Koch, D., & Salyk, C. (2006). Modeling production and climate-related impacts on ^{10} Be concentration in ice cores. *Journal of Geophysical Research*, *111*, D15107. https://doi.org/10.1029/2005jd006410

Golubenko, K., Rozanov, E., Kovaltsov, G., Leppänen, A.-P., Sukhodolov, T., & Usoskin, I. (2021). Chemistry-climate model SOCOL-AERv2-BEv1 with the cosmogenic beryllium-7 isotope cycle. *Geoscientific Model Development Discussions*, *2021*, 1–24. Retrieved from https://gmd.copernicus.org/preprints/gmd-2021-56/

Golubenko, K., Rozanov, E., Sukhodolov, T., & Usoskin, I. (2021). CCM SOCOL-AERv2-BEv1. [Software]. Zenodo. https://doi.org/10.5281/zenodo.5006356

Golubenko, K., Usoskin, I., Rozanov, E., & Kovaltsov, G. (2022). Simulations of cosmogenic isotopes production via CCM SOCOL-AERv2-BE. [Datasets]. Zenodo. https://doi.org/10.5281/zenodo.4696224

Heikkilä, U., Beer, J., Abreu, J. A., & Steinhilber, F. (2013). On the atmospheric transport and deposition of the cosmogenic radionuclides (^{10}Be): A review. *Space Science Reviews*, *176*, 321–332. https://doi.org/10.1007/s11214-011-9838-0

Heikkilä, U., Beer, J., & Alfimov, V. (2008). Beryllium-10 and beryllium-7 in precipitation in dübendorf (440 m) and at jungfraujoch (3580 m), Switzerland (1998–2005). *Journal of Geophysical Research*, *113*(D11), D11104. https://doi.org/10.1029/2007JD009160

Heikkilä, U., Beer, J., & Feichter, J. (2009). Meridional transport and deposition of atmospheric ^{10}Be. *Atmospheric Chemistry and Physics*, *9*, 515–527. https://doi.org/10.5194/acp-9-515-2009

Heikkilä, U., Muscheler, R., & Smith, A. M. (2013). Phase of solar activity affects response of solar proxy ^{10}Be. *Earth and Planetary Science Letters*, *380*, 72–76. https://doi.org/10.1016/j.epsl.2013.08.036

Herbst, K., Kopp, A., & Heber, B. (2013). Influence of the terrestrial magnetic field geometry on the cutoff rigidity of cosmic ray particles. *Annales Geophysicae*, *31*(10), 1637–1643. https://doi.org/10.5194/angeo-31-1637-2013

Herbst, K., Kopp, A., Heber, B., Steinhilber, F., Fichtner, H., Scherer, K., & Matthiä, D. (2010). On the importance of the local interstellar spectrum for the solar modulation parameter. *Journal of Geophysical Research*, *115*, D00I20. https://doi.org/10.1029/2009JD012557

Hersbach, H., Bell, B., Berrisford, P., Hirahara, S., Horányi, A., Muñoz-Sabater, J., et al. (2020). The era5 global reanalysis. *Quarterly Journal of the Royal Meteorological Society*, *146*(730), 1999–2049. https://doi.org/10.1002/qj.3803

Hommel, R., Timmreck, C., & Graf, H. F. (2011). The global middle-atmosphere aerosol model MAECHAM5-SAM2: Comparison with satellite and in-situ observations. *Geoscientific Model Development*, *4*(3), 809–834. https://doi.org/10.5194/gmd-4-809-2011

Keeling, R. F., Graven, H. D., Welp, L. R., Resplandy, L., Bi, J., Piper, S. C., et al. (2017). Atmospheric evidence for a global secular increase in carbon isotopic discrimination of land photosynthesis. *Proceedings of the National Academy of Sciences of the United States of America*, *114*(39), 10361–10366. Retrieved from https://www.pnas.org/content/114/39/10361

Koldobskiy, S. A., Bindi, V., Corti, C., Kovaltsov, G. A., & Usoskin, I. G. (2019). Validation of the neutron monitor yield function using data from AMS-02 experiment 2011 – 2017. *Journal of Geophysical Research*, *124*, 2367–2379. https://doi.org/10.1029/2018JA026340

Koldobskiy, S. A., Raukunen, O., Vainio, R., Kovaltsov, G., & Usoskin, I. (2021). New reconstruction of event-integrated spectra (spectral fluences) for major solar energetic particle events. *Astronomy & Astrophysics*, *647*, A132. https://doi.org/10.1051/0004-6361/202040058

Koldobskiy, S. A., Usoskin, I., & Kovaltsov, G. (2022). Effective energy of cosmogenic isotope (^{10}Be, ^{14}C and ^{36}Cl) production by solar energetic particles and galactic cosmic rays. *Journal of Geophysical Research: Space Physics*, *127*, e2021JA029919. https://doi.org/10.1029/2021JA029919

Korschinek, G., Bergmaier, A., Faestermann, T., Gerstmann, U. C., Knie, K., Rugel, G., et al. (2010). A new value for the half-life of ^{10}Be by Heavy-Ion Elastic Recoil Detection and liquid scintillation counting. *Nuclear Instruments and Methods in Physics Research Section B*, *268*(2), 187–191. https://doi.org/10.1016/j.nimb.2009.09.020

Kovaltsov, G., Mishev, A., & Usoskin, I. (2012). A new model of cosmogenic production of radiocarbon ^{14}C in the atmosphere. *Earth and Planetary Science Letters*, *337*, 114–120. https://doi.org/10.1016/j.epsl.2012.05.036

Kovaltsov, G., & Usoskin, I. (2010). A new 3D numerical model of cosmogenic nuclide ^{10}Be production in the atmosphere. *Earth and Planetary Science Letters*, *291*, 182–188. https://doi.org/10.1016/j.epsl.2010.01.011

Lal, D., & Peters, B. (1967). Cosmic ray produced radioactivity on the earth. In K. Sittle (Ed.), *Handbuch der physik* (Vol. 46, pp. 551–612). Springer. https://doi.org/10.1007/978-3-642-46079-1_7

Leppänen, A.-P., Pacini, A. A., Usoskin, I. G., Aldahan, A., Echer, E., Evangelista, H., et al. (2010). Cosmogenic ^{7}Be in air: A complex mixture of production and transport. *Journal of Atmospheric and Solar-Terrestrial Physics*, *72*, 1036–1043. https://doi.org/10.1016/j.jastp.2010.06.006

Lingenfelter, R. (1963). Production of carbon 14 by cosmic-ray neutrons. *Reviews of Geophysics and Space Physics*, *1*, 35–55. https://doi.org/10.1029/rg001i001p00035

Masarik, J., & Beer, J. (1999). Simulation of particle fluxes and cosmogenic nuclide production in the earth's atmosphere. *Journal of Geophysical Research*, *104*, 12099–12111. https://doi.org/10.1029/1998jd200091

Masarik, J., & Beer, J. (2009). An updated simulation of particle fluxes and cosmogenic nuclide production in the Earth's atmosphere. *Journal of Geophysical Research*, *114*, D11103. https://doi.org/10.1029/2008JD010557

McCracken, K. (2004). Geomagnetic and atmospheric effects upon the cosmogenic ^{10}Be observed in polar ice. *Journal of Geophysical Research*, *109*(A18), A04101. https://doi.org/10.1029/2003JA010060

Mekhaldi, F., Adolphi, F., Herbst, K., & Muscheler, R. (2021). The signal of solar storms embedded in cosmogenic radionuclides: Detectability and uncertainties. *Journal of Geophysical Research*, *126*(8), e29351. https://doi.org/10.1029/2021JA029351

Mekhaldi, F., Muscheler, R., Adolphi, F., Aldahan, A., Beer, J., McConnell, J., et al. (2015). Multiradionuclide evidence for the solar origin of the cosmic-ray events of AD 774/5 and 993/4. *Nature Communications*, *6*, 8611. https://doi.org/10.1038/ncomms9611

Meng, L., Liu, J., Tarasick, D. W., Randel, W. J., Steiner, A. K., Wilhelmsen, H., et al. (2021). Continuous rise of the tropopause in the Northern Hemisphere over 1980 – 2020. *Science Advances*, *7*(45), eabi8065. https://doi.org/10.1126/sciadv.abi8065

Miyake, F., Masuda, K., & Nakamura, T. (2013). Another rapid event in the carbon-14 content of tree rings. *Nature Communications*, *4*, 1748. https://doi.org/10.1038/ncomms2783

Miyake, F., Nagaya, K., Masuda, K., & Nakamura, T. (2012). A signature of cosmic-ray increase in ad 774-775 from tree rings in Japan. *Nature*, *486*, 240–242. https://doi.org/10.1038/nature11123

Miyake, F., Usoskin, I., & Poluianov, S. (Eds.), (2019). *Extreme solar particle storms: The hostile sun*. IOP Publishing. https://doi.org/10.1088/2514-3433/ab404a

O'Brien, K. (1979). Secular variations in the production of cosmogenic isotopes in the earth's atmosphere. *Journal of Geophysical Research*, *84*, 423–431.

O'Hare, P., Mekhaldi, F., Adolphi, F., Raisbeck, G., Aldahan, A., Anderberg, E., et al. (2019). Multiradionuclide evidence for an extreme solar proton event around 2,610 B.P. (660 BC). *Proceedings of the National Academy of Sciences of the United States of America*, *116*(13), 5961–5966. https://doi.org/10.1073/pnas.1815725116

Oeschger, H., Siegenthaler, U., Schotterer, U., & Gugelmann, A. (1975). A box diffusion model to study the carbon dioxide exchange in nature. *Tellus*, *27*, 168–192. https://doi.org/10.3402/tellusa.v27i2.9900

Paleari, C., Mekhaldi, F., Adolphi, F., Christl, M., Vockenhuber, C., Gautschi, P., et al. (2022). Cosmogenic radionuclides reveal an extreme solar particle storm near a solar minimum 9125 years bp. *Nature Communications*, *13*, 214. https://doi.org/10.1038/s41467-021-27891-4

Poluianov, S., Kovaltsov, G. A., Mishev, A. L., & Usoskin, I. G. (2016). Production of cosmogenic isotopes ^{7}Be, ^{10}Be, ^{14}C, ^{22}Na, and ^{36}Cl in the atmosphere: Altitudinal profiles of yield functions. *Journal of Geophysical Research*, *121*, 8125–8136. https://doi.org/10.1002/2016JD025034

Poluianov, S., Kovaltsov, G. A., & Usoskin, I. G. (2020). A new full 3-D model of cosmogenic tritium ^{3}H production in the atmosphere (CRAC:3H). *Journal of Geophysical Research*, *125*(18), e33147. https://doi.org/10.1029/2020JD033147

Roth, R., & Joos, F. (2013). A reconstruction of radiocarbon production and total solar irradiance from the Holocene ^{14}C and CO_2 records: Implications of data and model uncertainties. *Climate of the Past*, *9*, 1879–1909. https://doi.org/10.5194/cp-9-1879-2013

Santer, B. D., Wehner, M. F., Wigley, T. M. L., Sausen, R., Meehl, G. A., Taylor, K. E., et al. (2003). Contributions of anthropogenic and natural forcing to recent tropopause height changes. *Science*, *301*(5632), 479–483. https://doi.org/10.1126/science.1084123

Schrijver, C. J., Beer, J., Baltensperger, U., Cliver, E., Güdel, M., Hudson, H., et al. (2012). Estimating the frequency of extremely energetic solar events, based on solar, stellar, lunar, and terrestrial records. *Journal of Geophysical Research*, *117*, A08103. https://doi.org/10.1029/2012JA017706

Simpson, J. A. (1960). The production of tritons and C^{14} in the terrestrial atmosphere by solar protons. *Journal of Geophysical Research*, *65*, 1615. https://doi.org/10.1029/JZ065i005p01615

Stenke, A., Schraner, M., Rozanov, E., Egorova, T., Luo, B., & Peter, T. (2013). The SOCOL version 3.0 chemistry-climate model: Description, evaluation, and implications from an advanced transport algorithm. *Geoscientific Model Development*, *6*(5), 1407–1427. https://doi.org/10.5194/gmd-6-1407-2013

Sukhodolov, T., Usoskin, I., Rozanov, E., Asvestari, E., Ball, W., Curran, M., et al. (2017). Atmospheric impacts of the strongest known solar particle storm of 775 AD. *Scientific Reports*, *7*, 45257. https://doi.org/10.1038/srep45257

Thébault, E., Finlay, C. C., Beggan, C. D., Alken, P., Aubert, J., Barrois, O., et al. (2015). International geomagnetic reference field: The 12th generation. *Earth Planets and Space*, *67*, 79. https://doi.org/10.1186/s40623-015-0228-9

Usoskin, I., & Kromer, B. (2005). Reconstruction of the ^{14}c production rate from measured relative abundance. *Radiocarbon*, *47*, 31–37. https://doi.org/10.1017/s0033822200052176

Usoskin, I. G., Alanko-Huotari, K., Kovaltsov, G. A., & Mursula, K. (2005). Heliospheric modulation of cosmic rays: Monthly reconstruction for 1951–2004. *Journal of Geophysical Research*, *110*, A12108. https://doi.org/10.1029/2005JA011250

Usoskin, I. G., Bazilevskaya, G. A., & Kovaltsov, G. A. (2011). Solar modulation parameter for cosmic rays since 1936 reconstructed from ground-based neutron monitors and ionization chambers. *Journal of Geophysical Research*, *116*, A02104. https://doi.org/10.1029/2010JA016105

Usoskin, I. G., Gallet, Y., Lopes, F., Kovaltsov, G. A., & Hulot, G. (2016). Solar activity during the Holocene: The Hallstatt cycle and its consequence for grand minima and maxim. *Astronomy & Astrophysics*, *587*, A150. https://doi.org/10.1051/0004-6361/201527295

Usoskin, I. G., Koldobskiy, S., Kovaltsov, G., Rozanov, E., Sukhodolov, T., Mishev, A., & Mironova, I. (2020). Revisited reference solar proton event of 23 February 1956: Assessment of the cosmogenic-isotope method sensitivity to extreme solar events. *Journal of Geophysical Research*, *125*(6), e27921. https://doi.org/10.1029/2020JA027921

Usoskin, I. G., & Kovaltsov, G. A. (2006). Cosmic ray induced ionization in the atmosphere: Full modeling and practical applications. *Journal of Geophysical Research*, *111*, D21206. https://doi.org/10.1029/2006JD007150

Usoskin, I. G., & Kovaltsov, G. A. (2008). Production of cosmogenic ^{7}Be isotope in the atmosphere: Full 3D modelling. *Journal of Geophysical Research*, *113*, D12107. https://doi.org/10.1029/2007JD009725

Usoskin, I. G., Kromer, B., Ludlow, F., Beer, J., Friedrich, M., Kovaltsov, G. A., et al. (2013). The AD775 cosmic event revisited: The Sun is to blame. *Astronomy & Astrophysics*, *552*, L3. https://doi.org/10.1051/0004-6361/201321080

Usoskin, I. G., Solanki, S., Kovaltsov, G., Beer, J., & Kromer, B. (2006). Solar proton events in cosmogenic isotope data. *Geophysical Research Letters*, *33*, L08107. https://doi.org/10.1029/2006GL026059

Uusitalo, J., Arppe, L., Hackman, T., Helama, S., Kovaltsov, G., Mielikäinen, K., et al. (2018). Solar superstorm of AD 774 recorded subannually by Arctic tree rings. *Nature Communications*, *9*, 3495. https://doi.org/10.1038/s41467-018-05883-1

Vos, E. E., & Potgieter, M. S. (2015). New modeling of galactic proton modulation during the minimum of solar cycle 23/24. *The Astrophysical Journal*, *815*, 119. https://doi.org/10.1088/0004-637X/815/2/119

Webber, W., & Higbie, P. (2003). Production of cosmogenic be nuclei in the earth's atmosphere by cosmic rays: Its dependence on solar modulation and the interstellar cosmic ray spectrum. *Journal of Geophysical Research*, *108*, 1355. https://doi.org/10.1029/2003JA009863

Webber, W., Higbie, P., & McCracken, K. (2007). Production of the cosmogenic isotopes ^{3}H, ^{7}Be, ^{10}Be, and ^{36}Cl in the Earth's atmosphere by solar and galactic cosmic rays. *Journal of Geophysical Research*, *112*, A10106. https://doi.org/10.1029/2007JA012499

Wu, C. J., Usoskin, I. G., Krivova, N., Kovaltsov, G. A., Baroni, M., Bard, E., & Solanki, S. K. (2018). Solar activity over nine millennia: A consistent multi-proxy reconstruction. *Astronomy & Astrophysics*, *615*, A93. https://doi.org/10.1051/0004-6361/201731892